Shyr-Long Jeng
Graduate Research Assistant.

Wei-Hua Chieng
Associate Professor.

An-Chen Lee
Professor.

Department of Mechanical Engineering,
National Chiao-Tung University,
Hsin-Chu, Taiwan 30049

Modeling and Diagnosis of Motion Error of Multi-Axis Machines Using a Ball Bar Test

The contouring accuracy of a multi-axis machine has a critical effect on the quality of many advanced technology products. One of the best approaches to assessing the contouring performance of machine tools is through double ball bar measurement. During circular interpolation motion, the machine traverses, with two axes at a time, a circular trajectory, with each axis subject to sinusoidal changes in acceleration, velocity, and position. The motion error is measured by detecting the relative distance between a point on the spindle nose and another point on the machine table and plotting this distance in polar coordinates. The present paper derives mathematical models and diagnosis procedures for first and second-order motion error resulting from the active degrees of freedom of a multi-axis machine. The theoretical results are verified by both computer simulation and double ball bar testing experiments.

1 Introduction

Many types of measuring tools, such as coordinate measuring machines and laser interferometers, can be used for precision measurement. Coordinate measuring machines essentially consist of a means of moving a probe or part within a three-dimensional rectilinear coordinate system. They accurately establish and record the spatial coordinate location of selected contact points. Laser interferometers are commonly used to determine the accuracy of machine tool elements.

The DBB (double ball bar) measurement system is less expensive than the above measuring tools and more suitable for quick-check purposes. The error patterns obtained from the DBB measurement involve not only individual leadscrew inaccuracy but also geometric error, such as Abbe error (Zhang, 1989), and improper dynamic characteristics in the servo-loops (Poo, 1972; Koren, 1980). Bryan (1982) presented an error diagnosis method for measuring geometric error based on a magnetic double ball bar. Knapp (1983) studied the relation between the contouring error and the motion error sources. Kunzmann (1983) developed a two-dimensional characteristic matrix including squareness and longitudinal parameters to describe motion error. Kakino (1987) described various types of motion error using the notation of error vectors.

However, all of these methods are either too abstract or too incomplete to analyze motion error. In addition, a feasible diagnosis procedure has yet to be proposed in the literature. In this paper, we derive a complete mathematical model for most significant motion error with the DBB measuring tool. This mathematical model can be used as a basis for classifying individual error sources. In addition, we develop an innovative diagnosis procedure to determine the motion errors of multi-axis machines. Through different experimental setups, the diagnosis procedure can be used to analyze the motion error by incorporating both time domain and frequency domain data. Finally, the least-squares fitting method (Strange, 1980) is used to classify the individual motion error of a multi-axis machine.

The analysis and diagnosis procedures presented in this paper are mainly based on the XY trace. Alternatively, the traces on the ZX and YZ planes can also be used without much difficulty. In general, we employ the standard notation in (ASME B5.54, 1992). However, notation that is inadequate for double ball bar measurement has been redefined.

2 Mathematical Modeling of Motion Error

In DBB measurement, as shown in Fig. 1, the LVDT in the extension bar is used to detect the relative distance between the two ends of the balls. Applying circular interpolation motion with radius r_0, the contouring error ΔL is measured by subtracting the length of the extension bar L_1 between the fixed socket on the spindle node and the moving socket on the positioning table from the reference length L_0 of extension bar.

In the following, two different mathematical models, a linear model and a nonlinear model, to describe the motion error due to a faulty guideway system are provided. The linear model is based on a first-order approximation. In the linear model, the guideways are assumed to be linear, so deflection of the guideways will be ignored. In the nonlinear model, which uses a second-order approximation, the guideways are allowed to deflect.

As shown in Fig. 2(a), the total motion error can be seen as a combination of the error from the controller coordinates, through the guideway coordinates, to the world coordinates. In this paper, the superscript $'$ is used to denote the guideway coordinates and superscript $''$ is used to denote the controller coordinates.

Linear Model. Since we assume that the x and y guideways are linear, we can describe the geometric motion error with the Euler angles for each individual guideway given in the pitch-yaw-roll (or ϕ-θ-φ) sequence.

In the guideway coordinate system, the x', y', and z' axes are aligned with the x-guideway, y-guideway, and spindle axis, respectively. Without loss of generality, as shown in Fig. 1, we let the x guideway be mounted on top of the y guideway. For the DBB measurement, it is convenient to let the z axis of the world coordinate system coincide with the z' axis (spindle axis), and the y axis of the world coordinate system lie on the z-y' plane. The x axis of the world coordinate system can subsequently be obtained by applying the right-hand principle.

In order to let the y axis lie on the z-y' plane, we let the yaw angle θ_y be zero. As shown in Fig. 3, the relation between the unit vectors for the y' and y axes can be derived as follows:

$$\mathbf{y}' = \mathbf{R}(\varphi_y)\mathbf{R}(\phi_y)\mathbf{y} \qquad (1a)$$

Similarly, for the x guideway mounted on top of the y guideway,

Contributed by the Dynamic Systems and Control Division for publication in the JOURNAL OF DYNAMIC SYSTEMS, MEASUREMENT, AND CONTROL. Manuscript received by the DSCD August 18, 1993; revised manuscript received August 29, 1995. Associate Technical Editor: J. L. Stein.

Copyright © 1996 by ASME

Downloaded From: http://dynamicsystems.asmedigitalcollection.asme.org/ on 04/28/2014 Terms of Use: http://asme.org/terms

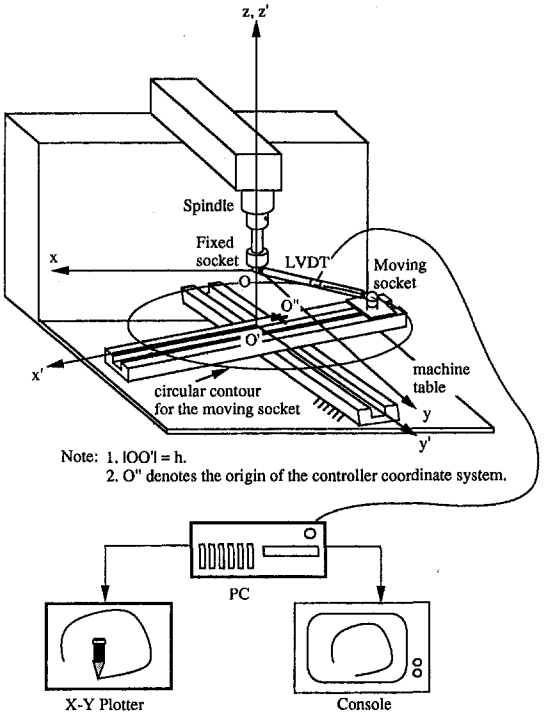

Fig. 1 Configuration for the circular contouring test experiment

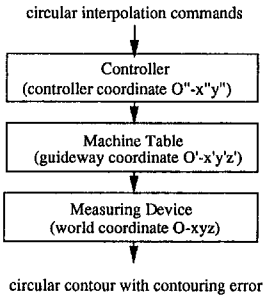

Fig. 2(a)

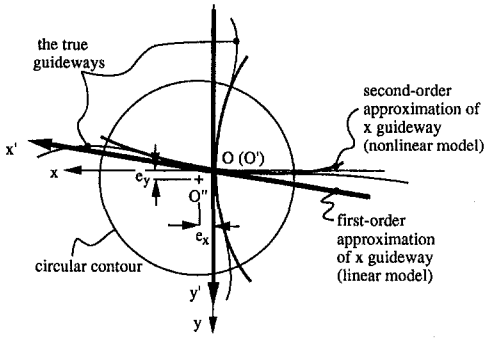

Fig. 2(b)

Fig. 2 (a) The coordinate transformations between different coordinate systems. (b) Top view of the local approximation scheme (view along the z axis). O coincides with O', and the y axis coincides with the y' axis. O" is the center of the circular motion.

the relation between the unit vectors $\mathbf{x}'$ and $\mathbf{x}$ can be expressed as follows:

$$\mathbf{x}' = \mathbf{R}(\varphi_y)\mathbf{R}(\phi_y)\mathbf{R}(\varphi_x)\mathbf{R}(\theta_x)\mathbf{R}(\phi_x)\mathbf{x} \qquad (1b)$$

The origin O of the world coordinate system is chosen to be the center of the fixed socket of the DBB, as shown in Fig. 1. The origin O' of the guideway coordinate system is chosen to be the projection of O along the z axis to the x'-y' plane. Rearranging Eq. (1a) and Eq. (1b), we can express the mapping from the guideway to the world coordinate system in matrix form as follows:

$$\begin{bmatrix} x \\ y \\ z \end{bmatrix} = \mathbf{R}\begin{bmatrix} x' \\ y' \\ 0 \end{bmatrix} + \begin{bmatrix} 0 \\ 0 \\ -h \end{bmatrix} \qquad (2a)$$

where h denotes the height of the center of the fixed socket from the center of the moving socket in the z direction. The rotational transformation matrix $\mathbf{R}$ can be derived as follows:

$$\mathbf{R} = \begin{bmatrix} \cos\theta_x \cos(\varphi_y + \phi_x) & 0 & 0 \\ \cos\phi_y \sin\theta_x + \sin\phi_y \cos\theta_x \sin(\varphi_y + \phi_x) & \cos\phi_y & 0 \\ \sin\phi_y \sin\theta_x - \cos\phi_y \cos\theta_x \sin(\varphi_y + \phi_x) & \sin\phi_y & 1 \end{bmatrix} \qquad (2b)$$

When all the Euler angles are equal to zero, the rotational matrix $\mathbf{R}$ yields an identity matrix. According to Eq. (2b), a ball bar measurement is subject to two limitations in: 1) φ_y and ϕ_x are coupled and cannot be measured individually, and 2) the roll angle φ_x of the x-axis cannot be determined when the height of the moving socket is neglected.

Nomenclature

x-y-z = world (absolute) coordinate system
x'-y'-z' = guideway coordinate system
x''-y''-z'' = controller coordinate system
e_x, e_y = center-offset error of x and y axes, respectively
h = height of the center of the fixed socket from the machine table
L_0 = reference distance between fixed and moving sockets
p_x, p_y = screw pitch of the x and y ball screw
$\mathbf{r}_f$, $\mathbf{r}_m$ = world coordinate of the fixed socket and the moving socket
$\mathbf{r}''_m$ = controller coordinates of $\mathbf{r}_m$
S_x, S_y = nominal scaling factor at x and y axes, respectively
ψ = closed-loop phase angle mismatching error
ϕ_x, ϕ_y = pitch angle error of the x and y axes for the linear model
φ_x, φ_y = roll angle error of the x and y axes for the linear model
θ_x, θ_y = yaw angle error of the x and y axes for the linear model
δ_x, δ_y = nominal backlash in the x and y axes, respectively
κ_{roll} = roll motion constant of the y-guideway for the nonlinear model
$\varphi_{x,\text{roll}}$ = initial roll angle of the y guideway for the nonlinear model
$\theta_{x,\text{yaw}}$ = initial yaw angle of the x guideway for the nonlinear model
$\phi_{x,\text{pitch}}$ = initial yaw angle of the x guideway for the nonlinear model
$\phi_{y,\text{pitch}}$ = initial yaw angle of the y guideway for the nonlinear model
$\rho_{x,\text{yaw}}$, $\rho_{y,\text{yaw}}$ = radius of curvature of the x and y axes for yaw motion error
$\rho_{x,\text{pitch}}$, $\rho_{y,\text{pitch}}$ = radius of curvature of the x and y axes for pitch motion error
$\theta_{\text{motor},x}$, $\theta_{\text{motor},yx}$ = rotation angle of the motor and encoder at x guideway
ζ = rotation angle of the circular motion

Downloaded From: http://dynamicsystems.asmedigitalcollection.asme.org/ on 04/28/2014 Terms of Use: http://asme.org/terms

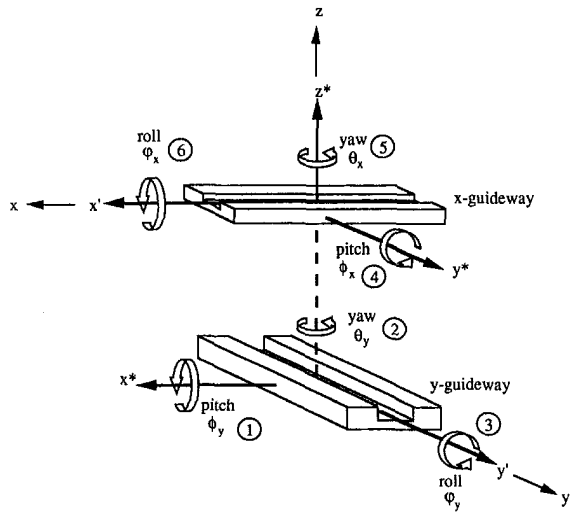

Note: 1. Numbers in the circles indicate the rotation sequence.
2. x' and y' are parallel to x and y, respectively, before rotation.

Fig. 3 The roll, pitch, and yaw angles of the guideways

If the measurement equipment is not set up properly, the origin of the guideway coordinate system may fail to coincide with the origin of the controller coordinate system by the offset distance e_x in the x direction and e_y in the y direction, as shown in Fig. 2(b). Therefore, the mapping between the controller coordinates and guideway coordinates may be expressed as follows:

$$\begin{cases} y' = S_y(y'' - e_y) \\ x' = S_x(x'' - e_x) \end{cases} \tag{3}$$

where S_x and S_y denote the nominal scale factors that may be induced by mismatching of the closed-loop gain.

Substituting Eq. (3) into Eq. (2a) and rearranging, we obtain the following mapping between controller coordinate system and world coordinate system:

$$\begin{bmatrix} x \\ y \\ z \end{bmatrix} = \mathbf{R} \begin{bmatrix} S_x & 0 & 0 \\ 0 & S_y & 0 \\ 0 & 0 & 1 \end{bmatrix} \begin{bmatrix} x'' - e_x \\ y'' - e_y \\ 0 \end{bmatrix} + \begin{bmatrix} 0 \\ 0 \\ -h \end{bmatrix} \tag{4}$$

The world coordinates and the controller coordinates of the moving socket are denoted by $\mathbf{r}_m$ and $\mathbf{r}''_m$, respectively. The trajectory of moving socket $\mathbf{r}''_m$ with circular motion is defined as follows:

$$\mathbf{r}''_m = \begin{bmatrix} r_0 \cos \zeta \\ r_0 \sin \zeta \\ 0 \end{bmatrix} \tag{5}$$

where r_0 denotes the input command of the nominal radius of the circular motion and ζ denotes the angle of the circular motion. Both of these parameters are fed into the NC controller as the command input. By substituting Eq. (5) into Eq. (4), we can obtain the position of the moving socket $\mathbf{r}_m$ in world coordinates:

$$\mathbf{r}_m = \mathbf{R} \begin{bmatrix} S_x & 0 & 0 \\ 0 & S_y & 0 \\ 0 & 0 & 1 \end{bmatrix} \begin{bmatrix} r_0 \cos \zeta - e_x \\ r_0 \sin \zeta - e_y \\ 0 \end{bmatrix} + \begin{bmatrix} 0 \\ 0 \\ -h \end{bmatrix} \tag{6}$$

Since the fixed socket is located at the origin of the world coordinate system, the contouring error, denoted by ΔL, can be derived as follows:

$$\Delta L = \|\mathbf{r}_m\| - L_0 \tag{7}$$

where L_0 is the reference length of the ball bar, expressed as follows:

$$L_0 = \sqrt{r_0^2 + h^2} \tag{8}$$

The characteristic functions of geometric motion errors may be obtained by using the Taylor series expansion of Eq. (7). In the following, we specify the types of geometric motion errors that may occur and derive their characteristic functions.

A. Center-Offset Error. If the measurement apparatus has been calibrated improperly, center-offset error, $e_x \neq 0$ or $e_y \neq 0$, may be induced. According to Eq. (7), the contouring error ΔL for the center-offset error e_x in the x direction, denoted by $\Delta L_{\text{offsetx}}$, may be expressed as follows:

$$\Delta L_{\text{offsetx}} = \sqrt{r_0^2 + h^2 + e_x^2 - 2e_x r_0 \cos \zeta} - L_0 \tag{9a}$$

From the Taylor series expansion of the above equation around $e_x = 0$, the first-order term of the contouring error ΔL is as follows:

$$\Delta L_{\text{offsetx}} \approx \frac{-r_0 e_x}{L_0} \cos \zeta \tag{9b}$$

Similarly, the contouring error ΔL due to center offset e_y in the y direction, denoted by $\Delta L_{\text{offsety}}$, can be obtained as follows:

$$\Delta L_{\text{offsety}} \approx \frac{-r_0 e_y}{L_0} \sin \zeta \tag{10}$$

B. Positioning Scale Error. The positioning scale error is induced mainly by the mismatching of ball screw scales or the mismatching of closed-loop gains. According to Eq. (7), the contouring error due to positioning scale error may be linearly approximated as follows:

$$\Delta L_{\text{SFx}} \approx \frac{r_0^2(S_x - 1)}{L_0} \cdot \frac{1 + \cos 2\zeta}{2} \tag{11}$$

The contouring error ΔL_{SFy} due to the position scale error S_y can be obtained in a similar manner.

C. Squareness Error. When the x and y guideways are not perpendicular, i.e., the x' axis is no longer perpendicular to the y' axis, squareness error occurs. The contouring error for infinitesimal θ_x can be obtained as follows:

$$\Delta L_{Pxy} \approx \frac{\theta_x r_0^2}{2L_0} \sin 2\zeta \tag{12}$$

D. Perpendicular Error (Squareness Error Associated With Z Axis). In this paper, the squareness error between the x' and z axes or between the y' and z axes is called the perpendicular error. The contouring error ΔL due to the perpendicular error about the x' and z axes, $\phi_x + \varphi_y \neq 0$, can be obtained as follows:

$$\Delta L_{Pxz} \approx \frac{hr_0(\phi_x + \varphi_y)}{L_0} \cos \zeta \tag{13}$$

Compared with Eq. (12) and Eq. (13), the characteristic function for perpendicular error differs from that for the squareness error. Similarly, the contouring error associated with the perpendicular error about the y' and z axes, $\phi_y \neq 0$, can be obtained using the same procedure.

Nonlinear Model. In the nonlinear model, the guideways are allowed to deflect. Consequently, the Euler angles are functions of the position of measurement. In order to clearly describe the deflective guideways, we use different parameters and notation. The yaw, pitch, and roll motion errors, for the deflective

Downloaded From: http://dynamicsystems.asmedigitalcollection.asme.org/ on 04/28/2014 Terms of Use: http://asme.org/terms

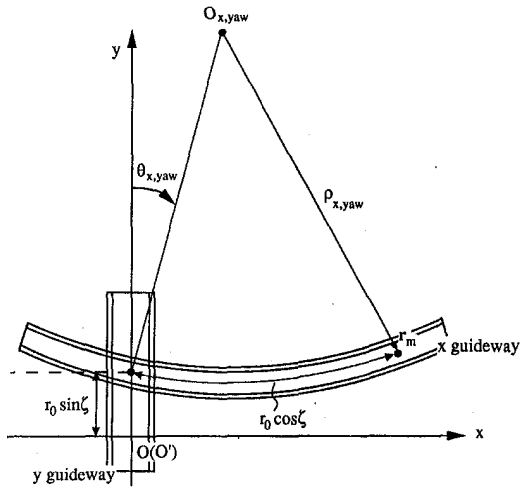

Fig. 4 Model for the yaw motion error of the *x* guideway

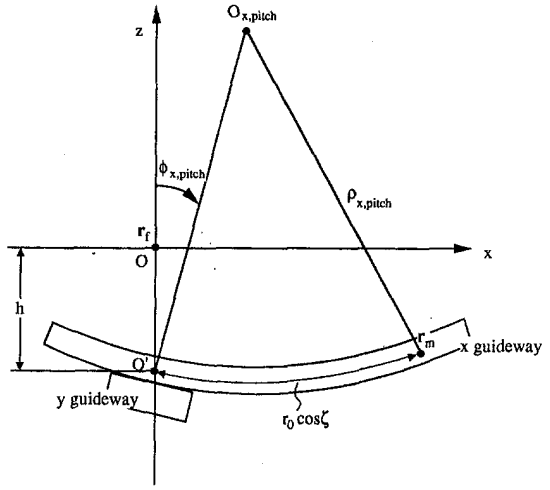

Fig. 5 The schematic diagram for pitch motion error of the *x* guideway

guideways are used instead of the squareness error and perpendicular error in the linear model.

A. Yaw Motion Error—Guideway Bending in *XY* Plane. When the guideway bends in the *XY* plane, the motion error induced is called yaw motion error. In Fig. 4, the *x* guideway is modeled by a circular arc with two independent parameters: the radius of curvature, denoted by $\rho_{x,yaw}$, and the initial yaw angle, denoted by $\theta_{x,yaw}$, which corresponds to the offset of the center of curvature $O_{x,yaw}$ from the *y* axis. During the circular motion, the world coordinates of the moving socket $\mathbf{r_m}$ can be directly formulated as follows:

$$\mathbf{r_m} = \begin{bmatrix} \rho_{x,yaw}\left(\sin\theta_{x,yaw} + \sin\left(\dfrac{r_0\cos\zeta}{\rho_{x,yaw}} - \theta_{x,yaw}\right)\right) \\ \rho_{x,yaw}\left(\cos\theta_{x,yaw} - \cos\left(\dfrac{r_0\cos\zeta}{\rho_{x,yaw}} - \theta_{x,yaw}\right)\right) + r_0\sin\zeta \\ -h \end{bmatrix} \tag{14}$$

Taking Eq. (14) into Eq. (7) and using the Taylor expansion around $\rho_{x,yaw} = \infty$ and $\theta_{x,yaw} = 0$, we can approximated the contouring error ΔL due to *x* yaw motion error, denoted by $\Delta L_{X,yaw}$, as follows:

$$\Delta L_{Xyaw} \approx \frac{r_0^3}{2\rho_{x,yaw}L_0}\sin\zeta\cos^2\zeta - \frac{r_0^2\theta_{x,yaw}}{L_0}\sin\zeta\cos\zeta \tag{15}$$

The first term of Eq. (15), a third-harmonic function, appears to be a special characteristic not found in the expressions for the motion errors. Comparing the second term of Eq. (15) with Eq. (12), we find that the initial yaw angle $\theta_{x,yaw}$ of the nonlinear model and the yaw angle θ_x of the linear model possess the same characteristic function.

When the *y* guideway bends about $O_{y,yaw}$, the contouring error ΔL_{Yyaw} can be derived in a manner similar to that used to derived Eq. (15). Recall that in the linear model we aligned the world coordinates so that the yaw angle θ_y would be zero. Similarly, in order to eliminate the rotational d.o.f. in the nonlinear model, we can rotate the world coordinate system so that $\theta_{y,yaw} = 0$.

B. Pitch Motion Error—Guideway Bends Toward *Z* Axis. As shown in Fig. 5, in this case the *x* guideway bends toward the center of curvature $O_{x,pitch}$ and the world coordinates of the moving socket $\mathbf{r_m}$ can be derived as follows:

$$\mathbf{r_m} = \begin{bmatrix} \rho_{x,pitch}\left(\sin\phi_{x,pitch} + \sin\left(\dfrac{r_0\cos\zeta}{\rho_{x,yaw}} - \phi_{x,pitch}\right)\right) \\ r_0\sin\zeta \\ \rho_{x,pitch}\left(\cos\phi_{x,pitch} - \cos\left(\dfrac{r_0\cos\zeta}{\rho_{x,yaw}} - \phi_{x,pitch}\right)\right) - h \end{bmatrix} \tag{16}$$

where $\rho_{y,pitch}$ denotes the radius of curvature and $\phi_{x,pitch}$, corresponding to the offset of the center of curvature $O_{x,pitch}$ from the *z* axis, denotes the initial pitch angle. Using the Taylor expansion around $\rho_{x,pitch} = \infty$ and $\phi_{x,pitch} = 0$, we can write the contouring error ΔL due to this type of motion error, ΔL_{Xpitch}, as follows:

$$\Delta L_{Xpitch} \approx \frac{-hr_0^2}{2\rho_{x,pitch}L_0}\cos^2\zeta + \frac{hr_0\phi_{x,pitch}}{L_0}\cos\zeta \tag{17}$$

Comparing the above equation with Eqs. (11) and (13), we find that the first term of the above equation has the same effect as the positioning scale error ΔL_{SF}. The second term is equivalent to the perpendicular error ΔL_{Pxz} described in the linear model. The contouring error ΔL_{Ypitch} due to the *y* guideway bending about $O_{y,pitch}$ may be derived in a similar manner.

C. Roll Motion Error—Guideway Twist Error. As shown in Fig. 6, let the guideway twist be modeled by two independent parameters, the twist constant κ_{roll} (radian/m) on the *y* guideway and the initial twist angle $\varphi_{y,roll}$:

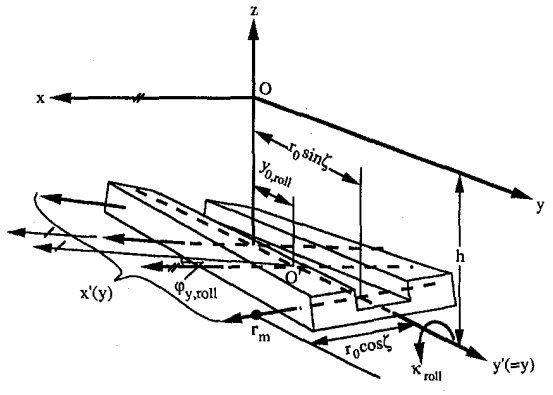

Fig. 6 Model for the roll motion error along the *y* guideway

Downloaded From: http://dynamicsystems.asmedigitalcollection.asme.org/ on 04/28/2014 Terms of Use: http://asme.org/terms

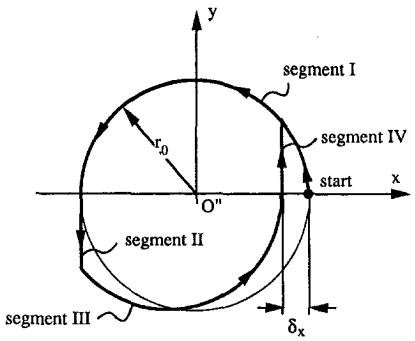

Fig. 7(a)

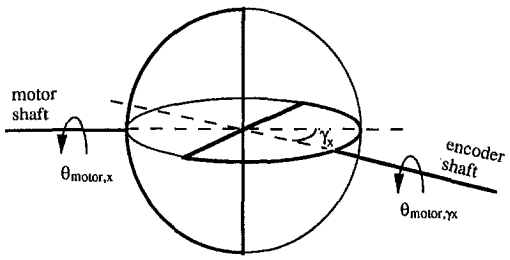

Fig. 7(b)

Fig. 7 (a) Distortion of the circular trajectory due to clearance error. (b) Schematic diagram of the indexing error.

$$\varphi_{y,\text{roll}} = \kappa_{\text{roll}} y_{0,\text{roll}} \tag{18a}$$

where the intermediate parameter $y_{0,\text{roll}}$ denotes the shift distance of the parallel axes. According to the geometry defined in Fig. 6, the contouring error ΔL due to the roll motion error, denoted by $\Delta L_{\gamma\text{roll}}$, can be linearly approximated by

$$\Delta L_{\gamma\text{roll}} \approx \frac{hr_0^2\kappa_{\text{roll}}}{2L_0} \sin 2\zeta - \frac{hr_0\varphi_{y,\text{roll}}}{L_0} \cos \zeta \tag{18b}$$

The contouring error shown in Eq. (18*b*) illustrates an effect similar to that of squareness error and perpendicular error in the linear model. Recall that in the linear model the roll angle φ_y cannot be decoupled from the pitch angle ϕ_x. Similarly, in the nonlinear model $\varphi_{y,\text{roll}}$ cannot be decoupled form $\phi_{x,\text{pitch}}$. Without loss of generality, we take $\varphi_{y,\text{roll}}$ to be zero in the later diagnosis procedures.

Other Motion Errors. In the following, we will derive the characteristic functions for the other types of motion errors. These motion errors may be incorporated within both the linear model and the nonlinear model.

A. Clearance Error. The clearance error may occur for a number of reasons, such as leadscrew backlash, lost motion of the driving system, and clearance in the guideways. The contouring error due to the clearance δ_x in the x direction may be analyzed by counter-clockwise (CCW) and clockwise (CW) tracing. When CCW tracing is used, as shown in Fig. 7(*a*), the contouring error under the existing clearance δ_x may be divided into four segments:

Segment I: $0° \le \zeta \le 180$ deg; $\mathbf{r_m}$ moves along the right circle. There is no contouring error in this segment.

$$\Delta L_{\text{CLR}x} = 0 \tag{19a}$$

Segment II: 180 deg $\le \zeta \le$ 180 deg + ζ_{CLR}: $\mathbf{r_m}$ remains unchanged. The contouring error is

$$\Delta L_{\text{CLR}x} = \sqrt{r_0^2 + r_0^2 \sin^2 \zeta + h^2} - L_0 \tag{19b}$$

Segment III: 180 deg + $\zeta_{\text{CLR}} \le \zeta \le$ 360 deg; the trajectory switches into another circular path. This effect is similar to the center-offset error.

$$\Delta L_{\text{CLR}x} = \sqrt{r_0^2 + \delta_x^2 + h^2 - 2r_0\delta_x \cos \zeta} - L_0 \tag{19c}$$

Segment IV: 360 deg $\le \zeta \le$ 360 + ζ_{CLR}: $\mathbf{r_m}$ remains unchanged. After this period, the tracking path re-enters the right circular path the same as in segment I. During this small period, the contouring error is

$$\Delta L_{\text{CLR}x} = \sqrt{(r_0 - \delta_x)^2 + r_0^2 \sin^2 \zeta + h^2} - L_0 \tag{19d}$$

By taking the Taylor series expansion around $\delta_x = 0$, the contouring error ΔL for the $\zeta_{\text{CLR}} \le \zeta \le 180$ and 180 deg + $\zeta_{\text{CLR}} \le \zeta \le$ 360 deg regions may be linearly approximated by

$$\Delta L_{\text{CLR}x} \approx \begin{cases} 0 & \zeta_{\text{CLR}} \le \zeta \le 180 \text{ deg} \\ \dfrac{-r_0\delta_x}{L_0} \cos \zeta & 180 \text{ deg} + \zeta_{\text{CLR}} \le \zeta \le 360 \text{ deg} \end{cases} \tag{20}$$

In a similar manner, the contouring error $\Delta L_{\text{CLR}x}$ for the clearance error δ_x with CW tracing and the contouring error $\Delta L_{\text{CLR}y}$ for the clearance error δ_y at the y axis with different directions of circular tracing may also be obtained.

B. Indexing Error. This error may occur because of misalignment between the encoder and motor shafts or pitch error in the screw driving system. In Fig. 7(*b*), the universal joint mechanism is used to illustrate indexing error. The input angle of the rotation of the motor is given by $\theta_{\text{motor},x}$, and the output angle is given by $\theta_{\text{motor},\gamma x}$. The relationship between the input and output angle can be expressed as

$$\theta_{\text{motor},\gamma x} = \tan^{-1} (\theta_{\text{motor},x} \cos \gamma_x) + \text{int}\left[\frac{\theta_{\text{motor},x}}{2\pi}\right] \tag{21}$$

where γ_x denotes the angle of misalignment of the encoder along the x guideway. Without going through the details, we present the contouring error as follows:

$$\Delta L_{\text{ENC}x} \approx \frac{-p_x r_0 \gamma_x^2 \cos \zeta \sin\left(\dfrac{4\pi r_0 \cos \zeta}{p_x}\right)}{8\pi L_0} \tag{22}$$

where p_x denotes the pitch of the x screw. According to the above equation, the indexing error induces the motion error with fairly high frequency compared with all other types of motion errors. In addition, the maximum motion error due to indexing error is less than 1 μm when the angle of misalignment is as large as 3° with $p_x = 5$ mm and $r_0 = L_0 = 150$ mm. Hence, in order to simplify the diagnosis process, this motion error can be ignored.

C. Mismatching of the Closed-Loop Phase Angles. Assume that the closed-loop response for the x and y servo driving system has no magnitude difference but that the phase difference is as follows:

$$\begin{cases} x'' = r_0 \cos (\omega t + \text{sgn}(\omega)\psi_x) \\ \quad = r_0 \cos (\zeta + \text{sgn}(\omega)\psi) \\ y'' = r_0 \sin (\omega t + \text{sgn}(\omega)\psi_y) = r_0 \sin \zeta \end{cases} \tag{23}$$

where $\zeta = \omega t + \text{sgn}(\omega)\psi_y$ and $\psi = \psi_x - \psi_y$. ψ_x and ψ_y denote the phase angles of the x servo driving response and y servo driving response, respectively. From the above equation, the contouring error ΔL_{PA} can be linearly approximated as follows:

Downloaded From: http://dynamicsystems.asmedigitalcollection.asme.org/ on 04/28/2014 Terms of Use: http://asme.org/terms

Table 1 The characteristic functions of different motion errors

Error	Characteristic Function	Harmonic order	Dependency h	Dependency sgn(ω)	model linear	model nonl.
Center-offset						
$\Delta L_{\text{offsetx}}$	$-\lambda\, e_x \cos\zeta$	1			√	√
$\Delta L_{\text{offsety}}$	$-\lambda\, e_y \sin\zeta$	1			√	√
Squareness						
ΔL_{Pxy}	$-\lambda\, \theta_x\, r_0 \sin 2\zeta / 2$	2			√	
Perpend.						
ΔL_{Pzx}	$-\lambda\, h\, (\phi_x+\varphi_y) \cos\zeta$	1	√		√	
ΔL_{Pyz}	$\lambda\, h\, \phi_y \sin\zeta$	1	√		√	
Clearance						
ΔL_{CLRx}	$-\lambda \text{sgn}(\omega)\delta_x \cos\zeta$ or 0	1*		√	√	√
ΔL_{CLRy}	$\lambda \text{sgn}(\omega)\delta_y \sin\zeta$ or 0	1*		√	√	√
Phase Angle Mismatching ΔL_{PA}	$-\lambda \text{sgn}(\omega) r_0 \psi \sin 2\zeta / 2$	2		√	√	√
Pos. Scale						
ΔL_{SFx}	$\lambda\, r_0\, (S_x - 1) \cos^2\zeta$	0, 2			√	√
ΔL_{SFy}	$\lambda\, r_0\, (S_y - 1) \sin^2\zeta$	0, 2			√	√
Roll motion ΔL_{Yroll}	$-\lambda h\, r_0\, \kappa_{roll} \sin 2\zeta / 2$	2	√			√
	$+\lambda h\, \varphi_{y,roll} \cos\zeta$	1	√			√
Pitch motion						
ΔL_{Xpitch}	$-\lambda h r_0 \cos^2\zeta / 2\rho_{x,pitch}$	0, 2	√			√
	$+\lambda h \phi_{x,pitch} \cos\zeta$	1	√			√
ΔL_{Ypitch}	$\lambda h r_0 \sin^2\zeta / 2\rho_{y,pitch}$	0, 2	√			√
	$-\lambda h\, \phi_{y,pitch} \sin\zeta$	1	√			√
Yaw motion						
ΔL_{Xyaw}	$-\lambda r_0^2 \sin\zeta \cos^2\zeta / 2\rho_{x,yaw}$	1, 3				√
	$+\lambda r_0 \theta_{x,yaw} \sin 2\zeta/2$	2				√
ΔL_{Yyaw}	$-\lambda r_0^2 \sin^2\zeta \cos\zeta / 2\rho_{y,yaw}$	1, 3				√

Note: $\lambda = \frac{r_0}{L_0}$

1*: the fundamental harmonic function in certain regions.

$$\Delta L_{PA} \approx \frac{-\text{sgn}(\omega) r_0^2 \psi}{2L_0} \sin 2\zeta \tag{24}$$

Equation (24) indicates that we may detect only the relative phase angle ψ in the contouring error. The servo-loop phase response of each individual axis cannot be obtained from DBB measurement.

3 Experimental Setup

Table 1 summarizes the characteristic functions of the various motion errors described above. According to Table 1, the characteristic functions for both the center-offset error and perpendicular error share the fundamental harmonic function of ζ. Similarly, the positioning scale error and pitch-motion error both include second-harmonic function of ζ. Because the center-offset error and the positioning scale error are independent of h, while the perpendicular error and the pitch motion error are not, we can perform two experiments with different values of h to identify these motion errors.

The squareness error and mismatching of the closed-loop phase angle are both independent of h and demonstrate the same harmonic function. Fortunately, the two motion errors may be identified by two circular tracings with different directions of rotation, because the contouring error of mismatching of the closed-loop phase angle is a function of the direction of circular tracing.

In summary, the individual motion errors in the linear model can be completely classified by either varying h or varying the direction of circular tracing. Hence, we conclude that when the linear model is used, two circular contouring tests are enough to distinguish all the motion errors.

Experiment #1: A circular test is performed to measure the contouring error with $h = 0$ and CCW tracing.

Experiment #2: A circular test is performed to measure the contouring error with $h \neq 0$ and CW tracing.

In the nonlinear model, three types of motion errors, $\theta_{x,yaw}$, ψ, and κ_{roll}, are coupled with the second-harmonic function, $\sin 2\zeta$. In order to classify these motion errors, one extra experiment is necessary:

Experiment #3: Repeat experiment #2 but with CCW tracing.

During the circular testing, the clearance error and stick-slip motion will enhance the complexity of the contouring error in the regions near $\zeta = 0$, 90, 180, and 270 deg. In order to facilitate the data processing and the corresponding analysis, the experimental data for these regions will be ignored.

Least-Squares Method. According the characteristic functions shown in Table 1, the problem of diagnosing the motion errors from various contouring error patterns can be transformed into a parameter estimation problem based on the least-squares method. For convenience, the estimated parameters may be rewritten in c symbols as shown below.

For the linear model, the fitting function may be expressed as follows:

$$y = \frac{-r_0^{(i)}}{L_0}\{c_1 \cos\zeta + c_2 \sin\zeta + c_3 h^{(i)} \cos\zeta - c_4 h^{(i)} \sin\zeta - c_5\,[\text{sgn}\,(\omega^{(i)}) \cos\zeta \text{ or } 0] - c_6\,[\text{sgn}\,(\omega^{(i)}) \sin\zeta \text{ or } 0] - c_7 r_0^{(i)} \cos^2\zeta - c_8 r_0^{(i)} \sin^2\zeta + c_9 r_0^{(i)} \sin 2\zeta + c_{10} r_0^{(i)} \sin 2\zeta\} \quad i = 1, 2, \ldots \tag{25}$$

where the index i indicates the ith experiment. The coefficients of the fitting function correspond to the motion errors as follows:

$$e_x = c_1, \quad e_y = c_2, \quad \phi_x + \varphi_y = c_3,$$
$$\phi_y = c_4, \quad \delta_x = c_5, \quad \delta_y = c_6$$
$$S_x = c_7 + 1, \quad S_y = c_8 + 1, \quad \theta_x = 2c_9, \quad \psi = 2c_{10}.$$

Similarly, the fitting function for the fifteen estimated parameters in the nonlinear model is

$$y = \frac{-r_0^{(i)}}{L_0}\{c_1 \cos\zeta + c_2 \sin\zeta - c_3[\text{sgn}\,(\omega^{(i)}) \cos\zeta \text{ or } 0] - c_4[\text{sgn}\,(\omega^{(i)}) \sin\zeta \text{ or } 0] - c_5 r_0^{(i)} \cos^2\zeta - c_6 r_0^{(i)} \sin^2\zeta + c_7 r_0^{(i)2} \sin^2\zeta \cos\zeta - c_8 r_0^{(i)2} \sin\zeta \cos^2\zeta + c_9 h^{(i)} r_0^{(i)} \cos^2\zeta - c_{10} h^{(i)} r_0^{(i)} \sin^2\zeta - c_{11} h^{(i)} \cos\zeta - c_{12} h^{(i)} \sin\zeta + c_{13} r_0^{(i)} \sin 2\zeta + c_{14}\,\text{sgn}\,(\omega^{(i)}) r_0^{(i)} \sin 2\zeta + c_{15} h^{(i)} \sin 2\zeta\} \quad i = 1, 2, 3, \ldots \tag{26}$$

The coefficients of the fitting function correspond to the motion errors as follows:

$$e_x = c_1, \quad e_y = c_2, \quad \delta_x = c_3, \quad \delta_y = c_4,$$
$$S_x = c_5 + 1, \quad S_y = c_6 + 1,$$
$$\rho_{y,yaw} = 1/(2c_7), \quad \rho_{x,yaw} = 1/(2c_8),$$
$$\rho_{x,pitch} = 1/(2c_9), \quad \rho_{y,pitch} = 1/(2c_{10}),$$
$$\phi_{x,pitch} = c_{11}, \quad \phi_{y,pitch} = c_{12}, \quad \theta_{x,yaw} = c_{13},$$
$$\psi = 2c_{14}, \quad \kappa_{roll} = 2c_{15}.$$

4 Computer Simulation

Consistency between the two different models is verified by the two sets of simulation reported in Table 2(a) and Table 2(b). Comparing the results shown in Table 2(b), we find that the errors estimated by both models are reasonably close to

Downloaded From: http://dynamicsystems.asmedigitalcollection.asme.org/ on 04/28/2014 Terms of Use: http://asme.org/terms

Table 2(*a*) Data settings in software simulation for error patter generation

Input Error Pattern	Height (mm)	Radius (mm)	Tracing Direction
#1	0.000	150.000	CCW
#2	30.000	146.969	CW
#3*	30.000	146.969	CCW

Note: #3 is used only with the nonlinear model.

Table 2(*b*) Diagnosis of motion error using input error patterns generated by simulator

Error Causes	Simulation (Given)	Linear Model	Nonlinear Model
e_x (μm)	-2.0	-2.005447	-2.005480
e_y (μm)	-3.0	-2.992325	-2.992323
δ_x (μm)	1.0	1.0011293	1.011372
δ_y (μm)	2.0	2.015433	2.015377
S_x	0.99999	0.99999	0.99999
S_y	1.00002	1.00002	1.00002
ψ	0.002°	0.002014°	0.0020136°
$\phi_x + \varphi_y$	0°	-0.000006°	
ϕ_y	0°	-0.000006°	
θ_x	0°	-0.000015°	
$\rho_{x,yaw}$ (m)	∞		1.03998e8
$\rho_{y,yaw}$ (m)	∞		-5.35248e8
$\rho_{x,pitch}$ (m)	∞		-79563.4
$\rho_{y,pitch}$ (m)	∞		115158
κ_{roll} (rad/m)	0 0		1.49217e-9
$\theta_{x,yaw}$ (rad)	0.0		-2.58813e-7
$\phi_{x,pitch}$ (rad)	0.0		1.02698e-7
$\varphi_{y,pitch}$ (rad)	0.0		-1.08139e-7

the prescribed error quantities. The numerical accuracy for the center-offset error and the backlash error of both models is within 0.01 μm. The numerical accuracy for perpendicular error or squareness error is around 0.00001 deg, which results in only a 0.01 μm difference in contouring error.

5 DBB Experiments

The experimental setup consisted of an industrial double ball bar on an industrial CNC machine center, as shown in Fig. 8. Contouring error data were collected in accordance with the procedures described above and plotted on polar or linear diagrams. Figure 9 and Fig. 10 show the experimental data and diagnosis results based on the linear and nonlinear model, respectively. The linear model required only two experiments, whereas the nonlinear model required at least three. Since the discrepancies are difficult to distinguish in the polar diagrams, auxiliary linear diagrams are also provided in the figures.

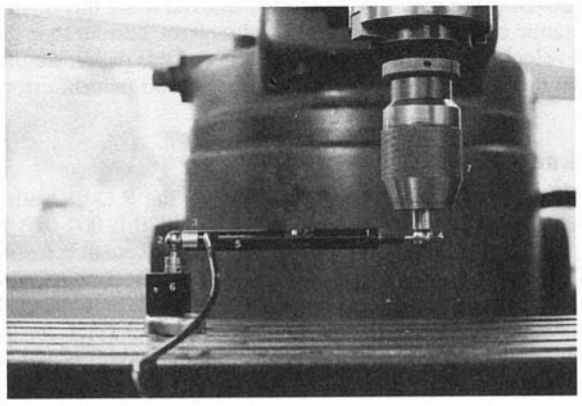

Fig. 8 Setup of the ball bar on the CNC machine tool.
Key:
1 Ball bar transducer
2 Ball joint (center mount)
3 Magnetic center cup
4 Magnetic tool cup
5 Extension bar
6 Magnetic center mount
7 Tool holder

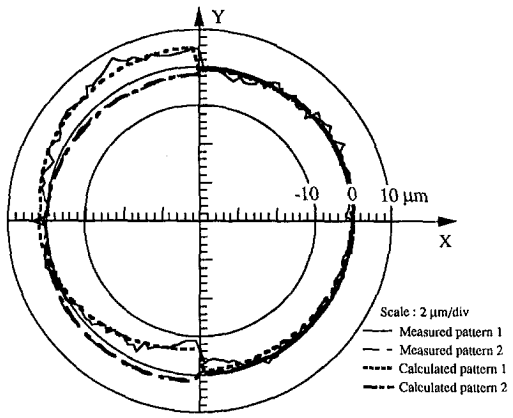

Fig. 9(*a*)

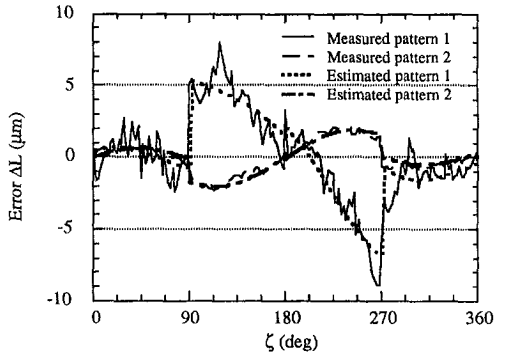

Fig. 9(*b*)

Fig. 9 Recognition of contouring error patterns based on linear model. (*a*) Polar diagram; (*b*) linear diagram.

Table 3 shows the numerical results of the diagnosis for both linear and nonlinear models. All the motion errors determined by the two models agree with each other, except for the center-offsets. Note that the roll-pitch-yaw motion error is significant compared with the data in Table 3. Consequently, a certain amount of contouring error has mistakenly been transferred to the components of the center-offset error in the linear model, which has less freedom for curve fitting. However, the maximum difference between the linear and nonlinear model is less than 0.3 μm of the center-offset error, so consistency in the diagnosis results for the two models is again obtained.

Because the characteristic functions of the motion errors are harmonic functions, much information is included in the frequency domain. Table 4 lists the magnitudes of the frequency responses at certain frequencies. Because the diagnosis is derived from the time domain, there is a certain amount of deviation between the experimental and the estimated patterns for the frequency components.

Comparisons Between Linear Model and Nonlinear Model. The linear model, which assumes that the guideways are straight, is independent of the position of measurement. In contrast, diagnosis results based on the nonlinear model will be a function of the position of measurement.

The advantage of the linear model is that the corresponding diagnosis may require as few as two input patterns with different

Downloaded From: http://dynamicsystems.asmedigitalcollection.asme.org/ on 04/28/2014 Terms of Use: http://asme.org/terms

Table 3(*a*) Settings in DBB experiment

Input Error Pattern	Height (mm)	Radius (mm)	Tracing Direction
#1	0.000	150.000	CCW
#2	144.568	40.000	CW
#3*	144.568	40.000	CCW

Note: #3 is used only with the nonlinear model.

Table 3(*b*) Diagnosis from DBB experimental data using linear and nonlinear models

Error Causes	Linear Model	Nonlinear Model
δ_x (μm)	0.814081	0.943694
δ_y (μm)	6.094524	5.965104
e_x (μm)	0.466008	0.171443
e_y (μm)	0.002037	-0.285577
S_x	1.000006	1.000006
S_y	0.999995	0.999995
ψ	0.003217°	0.004068°
$\phi_x + \varphi_y$	-0.000147°	
ϕ_y	-0.000069°	
θ_x	-0.003739°	
$\rho_{x,yaw}$ (m)		-13811.22
$\rho_{y,yaw}$ (m)		13484.75
$\rho_{x,pitch}$ (m)		-4708.9162
$\rho_{y,pitch}$ (m)		4680.379
κ_{roll} (rad/m)		1.589521e-4
$\theta_{x,yaw}$ (rad)		-7.87587e-5
$\phi_{x,pitch}$ (rad)		6.342634e-7
$\phi_{y,pitch}$ (rad)		-3.087036e-7

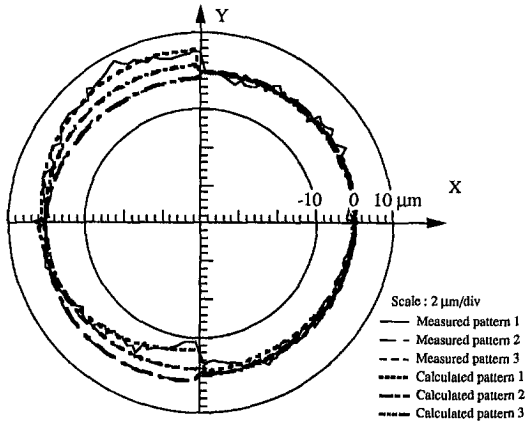

Fig. 10(*a*)

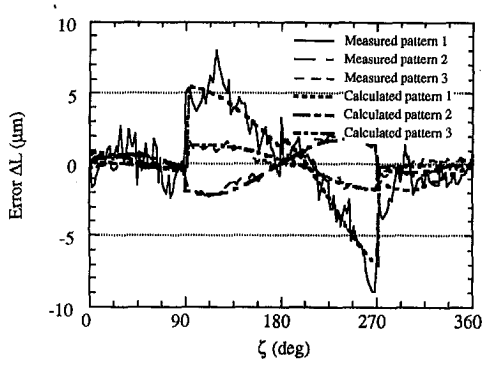

Fig. 10(*b*)

Fig. 10 Recognition of contouring error patterns based on the nonlinear model. (*a*) Polar diagram; (*b*) linear diagram.

Table 4 Frequency amplitude at certain frequencies

	× 0ω	× 1ω	× 2ω	× 3ω
Measured Pattern 1	48.4 dB	53.3 dB	51.9 dB	24.0 dB
Estimated Pattern1 (by Linear Model)	47.3 dB	52.2 dB	52.3 dB	18.4 dB
Estimated Pattern 1 (by Nonlinear Model)	47.1 dB	52.2 dB	52.3 dB	29.7 dB
Measured Pattern 2	15.9 dB	39.4 dB	47.7 dB	24.7dB
Estimated Pattern 1 (by Linear Model)	25.3 dB	40.1 dB	47.8 dB	14.18 dB
Estimated Pattern 2 (by Nonlinear Model)	25 dB	406 dB	48.1 dB	23.7 dB
Measured Pattern 3	37.9 dB	38.9 dB	41.9 dB	24.5 dB
Estimated Pattern 3 (by Nonlinear Model)	37.6 dB	39.8 dB	43.3 dB	21.7 dB

h and motion directions. Moreover, the linear model is less sensitive to numerical truncation error than the nonlinear model. The nonlinear model needs at least three input patterns and provides better estimation with a smaller variance in applications subject to a relatively large amount of motion error.

For practical applications, if the contouring error measured by the circular contouring test instrument is relatively small, then to minimize computing time as well as avoid numerical truncation error, the linear model is recommended. On the other hand, when the contouring error is sufficiently large or the contouring error induces a significantly large third-harmonic component in the frequency spectrum, the nonlinear model is preferred.

6 Conclusion

The characteristic functions for most NC motion errors have been modeled and analyzed using a linear and a nonlinear model. An analysis method and diagnosis procedures for the circular contouring test have also been introduced. With the diagnosis procedures, a variety of motion errors can be detected by means of the circular contouring test. The models described in this paper have been validated by tests on over twenty CNC machines at the R.O.C. Industrial Technology Research Institute (ITRI) and local CNC manufacturers. An average of 50 percent improvement in precision has been achieved using this modeler. Dynamic effects, such as the stick-slip effect, current loop gain, and velocity loop gain, which are neglected this paper, are likely to be the dominant factors in the unsolved 50 percent error.

Acknowledgments

This research was supported in part by the R.O.C. National Science Council under grant no. NSC 82-04220-E-009-072, and in part by the R.O.C. Industrial Technology Research Institute (ITRI) under grant no. C81028. In addition, the authors would like to thank Mr. Yee Song Chen, associated researched at ITRI, and Mr. Cheng-Hwei Chang, senior engineer at ITRI, for their enthusiastic assistance and guidance in the experimental and model validation sessions.

References

ASME B5.54, 1992, *Methods for Performance Evaluation of Computer Numerically Controlled Machining Center,* ASME, New York.

Bell, F., and Hemmelgarn, T., 1989, "Real Time Accuracy Enhancement for CMM's," *Proceedings of the ASPE Annual Meeting,* Atlanta.

Bryan, J. B., 1982, "A Simple Method for Testing Measuring Machine and Machine Tools," *Precision Engineering,* Vol. 4, No. 2, pp. 61–69.

Downloaded From: http://dynamicsystems.asmedigitalcollection.asme.org/ on 04/28/2014 Terms of Use: http://asme.org/terms

Kakino, Y., Ihara, Y., and Nakatsu, Y., 1987, "The Measurement of Motion Errors of NC Machine Tools and Diagnosis of Their Origins by Using Telescoping Magnetic Ball Bar Method," *Annals of the CIRP,* Vol. 36, pp. 377–383.

Knapp, W., 1983, "Test of the Three-Dimensional Uncertainty of Machine Tools and Measuring Machines and Its Relation to the Machine Errors," *Annals of the CIRP,* Vol. 32, pp. 459–464.

Koren, Y., 1980, "Cross-Coupled Biaxial Computer Control for Manufacturing Systems," ASME JOURNAL OF DYNAMIC SYSTEMS, MEASUREMENT, AND CONTROL, Vol. 102, No. 4, pp. 265–272.

Kunzmann, H., Waldele, F., and Bundesanstalt, P. T., 1983, "On Testing Coordinate Measuring Machines (CMM) with Kinematic Reference Standards (KRS)," *Annals of the CIRP,* Vol. 32, pp. 465–468.

Poo, A. N., Bollinger, J. G., and Younkin, G. W., 1972, "Dynamic Errors in Type 1 Contouring Systems," *IEEE Trans. on Industry Application,* Vol. IA-8, No. 4, pp. 477–484.

Strang, G., 1980, *Linear Algebra and Its Applications,* Academic Press, New York.

Zhang, G. X., 1989, "A Study on the Abbe Principle and Abbe Error," *Annals of CIRP,* Vol. 38, No. 1.

Downloaded From: http://dynamicsystems.asmedigitalcollection.asme.org/ on 04/28/2014 Terms of Use: http://asme.org/terms